Smart Materials and Structures

PAPER

A chip-sized piezoelectric receiver for low-frequency, near-field wireless power transfer: design, modeling and experimental validation

To cite this article: Miah A Halim *et al* 2021 *Smart Mater. Struct.* **30** 045011

View the article online for updates and enhancements.

This content was downloaded from IP address 128.227.1.40 on 04/03/2021 at 13:09

IOP Publishing Smart Materials and Structures
Smart Mater. Struct. **30** (2021) 045011 (11pp) https://doi.org/10.1088/1361-665X/abe60f

A chip-sized piezoelectric receiver for low-frequency, near-field wireless power transfer: design, modeling and experimental validation

Miah A Halim, Adrian A Rendon-Hernandez, Spencer E Smith and David P Arnold

Interdisciplinary Microsystems Group (IMG), University of Florida, Gainesville, FL 32611, United States of America

E-mail: md.miah@ufl.edu

Received 16 November 2020, revised 26 January 2021
Accepted for publication 12 February 2021
Published 1 March 2021

Abstract

This work presents the design, modeling and characterization of a chip-sized piezoelectric receiver for low-frequency, near-field wireless power transmission. Utilizing a laser micro-machined titanium suspension, one NdFeB magnet, and two PZT-5A piezo-ceramic patches, the receiver operates at its torsion mode mechanical resonance. Two unimorph piezo-ceramic transducers are designed to maximize the power density of the receiver while maintaining a low mechanical resonant frequency for low-frequency electrodynamic wireless power transmission. An equivalent lumped-element circuit model is used to model the system performance. A prototype device is fabricated, assembled and tested, and the experimental results are compared with the system model. The 0.08 cm^3 device generates a maximum of 360 μW average power at 1 cm distance from a transmitter coil operating at 724 Hz and below human head and torso exposure limits. This data corresponds to 4.2 mW cm^{-3} power density. Overall, this volume-efficient design offers a low-profile and compact footprint for potentially wirelessly charging wearable and bio-implantable devices.

Keywords: electrodynamic transduction, electro-mechanical coupling, laser micro-machining, torsional resonance, piezoelectric transducers, wireless power transfer (WPT)

(Some figures may appear in colour only in the online journal)

1. Introduction

Over the past decade, wireless power transfer (WPT) becomes an increasingly popular method of delivering power to an electronic system [1–3]. It provides a deterministic method for actively transferring power from a source (transmitters) to destinations (receivers) wirelessly while removing the burden of plugging in a charging cable. Recent progress in WPT techniques motivate new avenues of research in different applications e.g. portable electronic devices [4], electric vehicles [5], medical implants [6], Internet of Things sensors [7], unmanned aerial vehicles [8], and so on. Although many techniques, such as optical [9] and ultrasound [10] methods, have been demonstrated to transfer power wirelessly, wireless powering through radio-frequency electromagnetic waves is the most established one and can be categorized into either near-field (non-radiative) and far-field (radiative) approaches [11].

Near-field electromagnetic energy transfer approaches such as inductive, magnetic resonance or capacitive coupling between transmitters and receivers are mostly researched and utilized in commercial product development, especially in mobile, wearable and implantable biomedical devices applications [12]. These approaches make use of electro-magnetic

 © 2021 IOP Publishing Ltd Printed in the UK

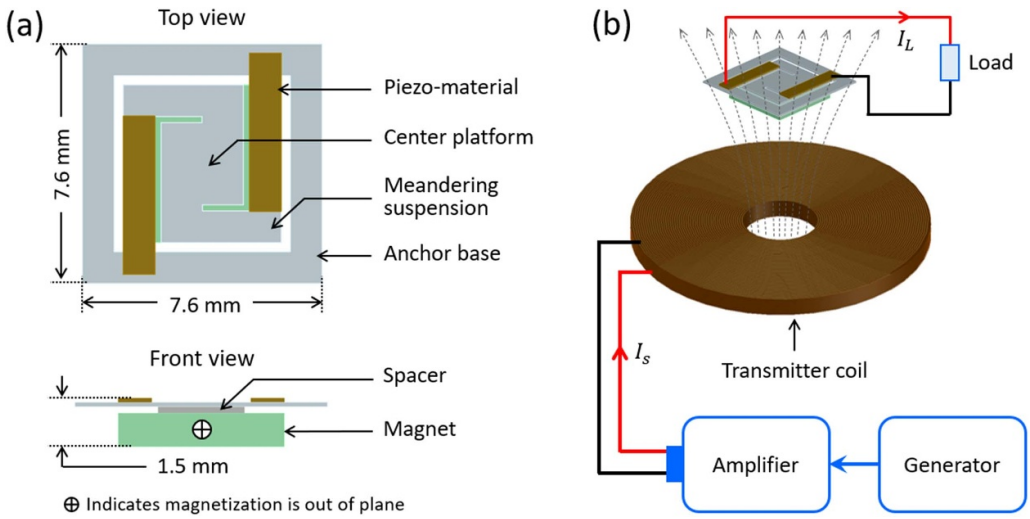

Figure 1. Schematics of the (a) piezoelectric electrodynamic wireless power transmission (EWPT) receiver structure and (b) the principle of EWPT operation.

fields within 0.1–10 MHz range and offer efficient power transmission over distances ranging from a few millimeter to several centimeters, depending on the size, structure, relative position and orientation, and the properties of the surrounding environment of the transmitter and receiver [13]. However, these near-field WPT technologies face unavoidable technical and safety concerns regarding the use of electromagnetic fields between the transmitter and receiver. In technical aspect, these relatively high-frequency inductively or capacitively coupled systems tend to generate eddy (Foucault) currents, in the case when the receiver is blocked by electrically conductive objects that attenuates or alters the electromagnetic fields being used for power transmission and can cause undesirable heating in the intervening objects [14]. The main safety concern, on the other hand, is the potential health hazard as there are strict limits to the amplitude of the electromagnetic fields that can be applied to humans [15, 16].

Low-frequency (<1 kHz) magnetic near-fields that uses electrodynamic coupling between a transmitter and a permanent magnet in a receiver have been considered as a possible solution to address these concerns [17, 18]. In principle, the receiver magnet oscillates (translational and/or rotational) when subjected to a time-varying magnetic field supplied from the transmitter which is then converted into electricity by one or more electromechanical transduction schemes such as electro-dynamic/induction, piezoelectric, or capacitive [19, 20]. This low-frequency electrodynamic WPT (EWPT) method facilitates higher field safety margins, and conceals the field attenuation and parasitic heating effects while transmitting through conductive media (e.g. metal, human body etc) [21]. For instance, an EWPT system using a rotating permanent magnet receiver demonstrated simultaneous charging of multiple wearable electronic devices in a cluttered environment [22]. Experimental demonstration of an EWPT receiver using precision manufactured electrodynamic transducer on a bulk micromachined silicon serpentine torsional suspension has been reported [23]. One challenge of a purely electrodynamic transduction in the receiver is that the induced voltages are typically quite small, e.g. <1 V that makes downstream ac/dc rectification and power management electronics very challenging. Consequently, piezoelectric transduction in the vibrating receiver element has also been explored. An EWPT piezoelectric receiver using a torsionally resonated meandering structure was experimentally demonstrated [24]. Model validation and analytical investigation of a piezoelectric cantilever based EWPT receivers was reported in [25], a more recent version of which utilizes a center-clamped bimorph piezoelectric cantilever beam with magnets attached at the two ends [26].

While great efforts have been exerted, all EWPT systems described above utilized relatively bulky receivers to demonstrate their functionalities. However, a much smaller design solution is needed for potential use in wearable and/or implantable applications. In this paper, we report a low-profile (1.5 mm), low-footprint (7.6×7.6 mm^2) EWPT receiver using a laser micro-machined suspension with significantly reduced volume that facilitates integration with modern printed circuit board electronics. Both finite element analysis (FEA) and lumped element modeling have been used to analyze the design, determine system parameters and predict the system performance. Finally, a prototype is fabricated and tested within the allowable human exposure limits, and the results are compared with the model.

2. Design and modeling

2.1. Receiver design

Figure 1 shows the schematics of the piezoelectric receiver structure and the principle of EWPT. As seen in figure 1(a), the receiver comprises a double-clamped (to the anchor base) meandering titanium suspension with a center platform, two piezo-ceramic patches attached to the clamped arms of the meandering beams, and a laterally magnetized

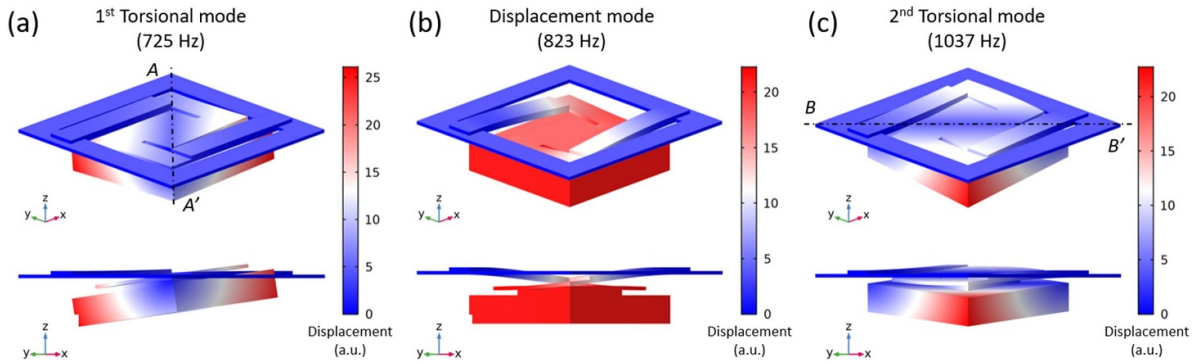

Figure 2. Modal analysis of the piezoelectric receiver to illustrate its mechanical resonance: (a) first torsional mode, (b) displacement mode, and (c) second torsional mode.

square permanent magnet mounted to the center platform (on the side opposite to the piezo-ceramic patches) via a spacer. The entire structure forms a resonant electromechanical transducer for power generation while oscillating torsionally under the influence of an external time-varying magnetic field. Titanium is selected for its high strength, lower mass (since lower mass springs develop less inertia as suspension is displaced), and the fact that is not ferromagnetic (so as to not interfere with the magnetic fields). Each piezo-ceramic patch constitutes a unimorph transducer and the piezos are connected electrically in series. For maximum electrodynamic coupling with the external magnetic field, the magnet spans the entire area over the meandering suspension. The spacer creates clearance between the magnet and the meandering beams during torsional oscillation. The external dimensions of the receiver are 7.6 mm $\times$ 7.6 mm, with a thickness of only 1.5 mm.

As illustrated in figure 1(b), an alternating current I_s supplied to a transmitter coil generates a spatially distributed, time-varying magnetic field of desired frequency and amplitude. When the receiver is subjected to this field, a torsional oscillation is induced due to torque on the receiver magnet. This motion generates dynamic stresses on the piezo-ceramic elements which, in turn, generate voltage by means of the piezoelectric effect. An electrical current I_L flows through an external load connected across the metal electrodes on the piezo-surfaces, and hence power is delivered. The voltage and power generated by the receiver are maximized at the torsional resonance of the mechanical suspension as well as when the magnetization axis of the receiver magnet is oriented perpendicular to the applied magnetic field.

The resonance behavior of the receiver is analyzed by FEA simulation using COMSOL MultiPhysics®. Figure 2 shows the modal analysis of the receiver to illustrate its mechanical resonances. To simulate the bonding layers (between the magnet, spacer and central platform, and between piezo-ceramic patches and suspension arms), a 20 μm-thick elastic layer with Young's modulus $E = 2$ GPa and Poisson's ratio $\nu = 0.25$ is used. The FEA simulations show that the first mode of vibration occurs at 725 Hz, which is a torsional rotation about the diagonal axis A–A′, the second mode of vibration at 823 Hz corresponds to a displacement mode in the z-direction, and the third mode of vibration at 1037 Hz is a torsional rotation about the diagonal axis B–B′.

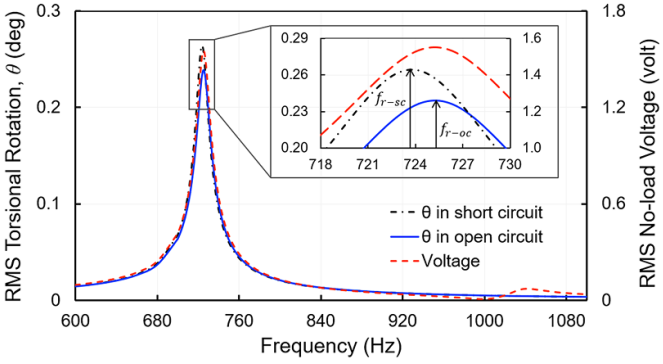

Figure 3. FEA simulated frequency response for the short-circuit and open-circuit torsional rotation angle about the diagonal axis A–A′ (see figure 2(a)), and the no-load voltage of the series connected piezoelectric transducers; the applied field is 50 μT_{rms} and the damping ratio $\zeta = 0.008$ ($Q = 60$).

As shown in figure 3, a frequency-domain FEA simulation is performed to investigate the frequency responses (both open-circuit and short-circuit) of the receiver for the torsional rotation angle θ about the diagonal axis A–A′. Additionally, the no-load (open-circuit) voltage of the series-connected piezoelectric transducers is simulated. For these simulations, an excitation magnetic field of 50 μT_{rms} is used along with a damping ratio $\zeta = 0.008$, corresponding to a Q-factor of 60 (as measured experimentally). At open-circuit, the oscillating receiver magnet reaches a maximum torsional rotation of 0.24° and correspondingly, maximum no-load (open-circuit) voltage at the first-mode torsional resonance $f_{r-oc} = 725.1$ Hz. At short-circuit, the resonance occurs at $f_{r-sc} = 723.6$ Hz.

In an effort to understand the mechanical reliability of the receiver, stress distribution simulations are performed; to that end, various magnetic field amplitude excitations at resonance are considered. Two mechanical limits are considered: (a) the maximum rotation angle at which the magnet comes in contact with the clamped arms of the meandering suspension (±3.25° for the present design) and (b) the threshold rotation angle where any portion of the suspension reaches its

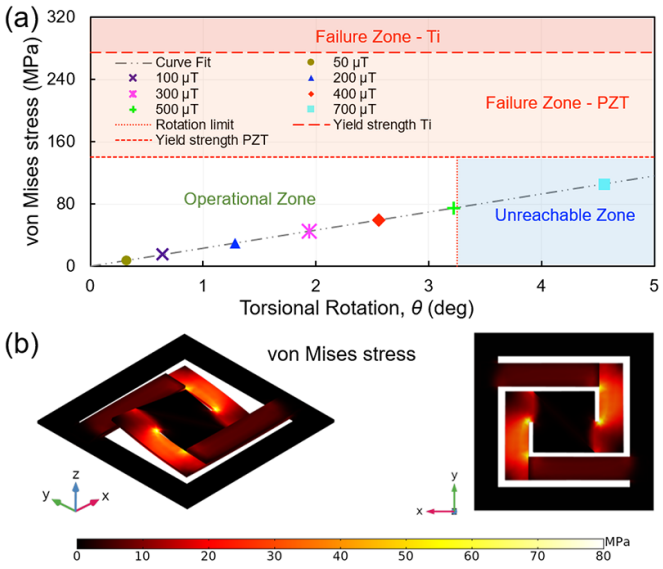

Figure 4. Mechanical reliability study via FEA simulation: (a) stress versus torsional rotation showing the operational, unreachable and failure zones, and (b) equivalent von Mises stress distribution on the suspension when an external field of 500 $\mu\mathrm{T_{rms}}$ is applied in dynamic loading at 725 Hz resonance (magnet and spacer not shown).

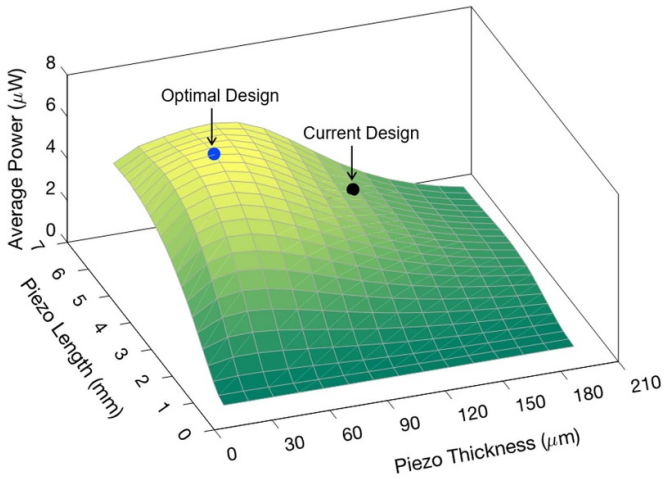

Figure 5. FEA simulation for the average power as function of length and thickness of each piezo-ceramic element; two piezoelectric transducers are in series with an adapted load resistance R_a, while 50 $\mu\mathrm{T_{rms}}$ is applied at corresponding first torsional mode resonance.

yield stress. Considering the ductility of titanium, it is assumed gradual failure mode would occur whenever the equivalent von Mises stress exceeds the tensile yield strength of titanium (assumed to be $\sigma_{\mathrm{YS-Ti}} = 275$ MPa). For the piezoelectric elements, we use the tensile yield strength of PZT-5A (assumed to be $\sigma_{\mathrm{YS-PZT}} = 140$ MPa). Figure 4(a) shows the failure diagram for the von Mises stress plotted against rotation angle. Here it is apparent that the magnet will interfere with the suspension base before exceeding one of the stress-related failure limits. As illustrated on figure 4(b), at the maximum rotation angle of $\pm 3.25°$, the maximum stress is only about 80 MPa, which is far below the failure limit for PZT-5A (or Ti).

For the design here, choosing appropriate dimensions of the piezoelectric elements is an essential design goal for maximizing the output power. The most important limitation lies in the fact that we integrated a commercial off-the-shelf piezoelectric element for which we can only adapt its length and width, not thickness that requires further processing of the piezoelectric material e.g. chemical mechanical polishing. With this in mind, a parametric FEA study is used to explore the output power response of the piezoelectric transducer while varying the length and thickness of the piezoelectric elements, as shown in figure 5. The width of the piezo is kept fixed at 1 mm (equal to the meander beam width), piezo length varies from 0.75 mm to 6 mm in steps of 0.25 mm, and piezo thickness varies from 13 μm to 195 μm in steps of 13 μm. Then, the resonant frequency of the first torsional mode of each receiver design is determined via FEA modal study. Following this, each receiver design is subjected to an applied field of 50 $\mu\mathrm{T_{rms}}$ at the corresponding first torsional mode resonance, and the output average power is calculated for an adapted load resistance $R_\mathrm{a} = 1/(2\pi f_\mathrm{a} C)$, where $f_\mathrm{a} = \sqrt{f_{\mathrm{r-sc}} f_{\mathrm{r-oc}}}$ and C is the capacitance of the series connected piezo-elements. In figure 5, one can note that the piezo length in the current design (5 mm) is very close to that of the optimal design (4.5 mm) however, a thinner 52 μm piezo thickness (127 μm in the current design) would maximize the receiver's output power.

2.2. *Lumped element equivalent circuit model*

Figure 6 shows the lumped-element electrical circuit model for the proposed EWPT system developed based on basic electromechanical transduction principles, and the electrical and mechanical equations of equilibrium [27, 28]. In this multi-energy-domain model, the three primary sections represent the electrical behavior of the transmitter, the mechanical behavior of the receiver (in this case, the rotational mechanics), and the electrical behavior of the receiver and load. Phasor voltages, currents, torques, and angular velocities are the primary system variables. In the first electrical domain, a power source with source resistance R_S supplies an ac voltage V_S and ac current I_S to a transmitter coil, represented by an electrical resistance R_T and inductance L_T. In the mechanical domain, the mechanical oscillator is represented by torsional damping coefficient b, mass moment of inertia J and short-circuit torsional spring stiffness k. Finally, in the second electrical domain, the blocked/clamped electrical capacitance of the piezoelectric transducer (assumed to be lossless) is represented by a capacitor C_0, and the output electrical terminals are connected to load impedance Z_L.

The electrodynamic transduction between the transmitter and receiver is represented by a gyrator with electrodynamic transduction coefficient K_T. The piezoelectric coupling of the piezo transducers is represented by a transformer with turns ratio Γ_P. The mechanical system oscillates at an angular velocity $\dot{\theta}$ in response to an electrodynamic torque τ_mag induced on the receiver magnet due to incoming magnetic fields from the transmitter coil. Note that, the magnetic fields produced by the

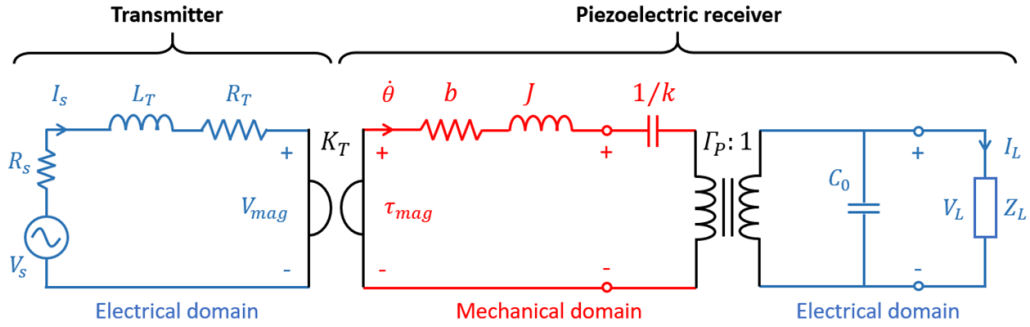

Figure 6. Equivalent electrical circuit representation of the EWPT system with piezoelectric receiver showing the energy flow between electrical and mechanical domains via electrodynamic and electromechanical couplings.

transmitter coil are not explicit in the equivalent circuit model, but will be discussed later. Due to the torsional motion of the mechanical system, an equivalent inertial force acts on the piezoelectric element (to the transverse direction) that results in developing strain in the piezo-material. This strain induces charges across the piezo-capacitor C_0 and hence, a voltage is generated. It is to be noted that the dielectric loss tangent of the piezoelectric material ($\tan\delta = 0.02$ at 1 kHz, provided on the manufacturer's datasheet) has negligible influence on the overall impedance and hence, is neglected in the model; at 1 kHz, the impedance of the parallel leakage resistance is $R_0 = 1/(2\pi f_t \tan\delta C) = 25$ MΩ, which is 50 times larger than the 0.5 MΩ piezo capacitance.

Generally, each lumped-element parameter can be derived using relevant geometric dimensions and material properties. However, due to the complicated design of the mechanical suspension and displacement (rotation/translation) of the central magnet mass, it is not easy to analytically derive all the standard lumped parameters for variables, particularly the torsional stiffness and rotational moment of inertia. Furthermore, some parameters (e.g. mechanical damping coefficient) are easier to determine by experimental measurements though. Therefore, a combination of COMSOL FEM results, analytical expressions, and experiments are used to determine all these lumped parameters, further discussed below.

2.3. System parameters

In the WPT system, the magnetic field produced by the transmitter coil (a multi-layer pancake type coil of inner diameter d_1, outer diameter d_2 and thickness l, having N turns) is modeled by a short-solenoid formula. The amplitude of the on-axis (refer to figure 1(b)) magnetic field is calculated as [18]

$$B_z = \frac{\mu_0 N I_S}{2l(d_2 - d_1)}\left[(l+2z)\ \ln\left(\frac{a_1}{a_2}\right) + (l-2z)\ \ln\left(\frac{a_3}{a_4}\right)\right] \quad (1)$$

where $a_1 = d_2 + \sqrt{d_2^2 + (l+2z)^2}$, $a_2 = d_1 + \sqrt{d_1^2 + (l+2z)^2}$, $a_3 = d_2 + \sqrt{d_2^2 + (l-2z)^2}$, $a_4 = d_1 + \sqrt{d_1^2 + (l-2z)^2}$, μ_0 ($=4\pi \times 10^{-7}$ N A^{-2}) is the permeability of free space, and z is the distance from the centroid of the transmitter coil. In order to maximize the torque acting on the receiver magnet, the magnetization axis of the magnet is oriented perpendicular to the magnetic field generated by the transmitter coil. Hence, the amount of torque induced on the receiver magnet is

$$\tau_{\text{mag}} = \left|\vec{m} \times \vec{B}_z\right| = \frac{B_r}{\mu_0} v_{\text{mag}} B_z \quad (2)$$

where $\vec{m} = \vec{M} v_{\text{mag}}$ is the net magnetic moment of the receiver magnet in which v_{mag} is the magnet volume and $\vec{M}$ is the magnetization of the magnet that is related to the remanence B_{r} of the magnet material as $\left|\vec{M}\right| = B_{\text{r}}/\mu_0$ (assuming ideal magnetization).

In addition to this torque, a pulling force also acts on the receiver magnet due to the magnetic field gradients produced by the transmitter coil, expresses as

$$\left|\vec{F}\right| = |\vec{m}|\frac{dB_z}{dz} \quad (3)$$

where $\frac{dB_z}{dz}$ is the magnetic field gradient in the z-direction. Since the rotation angle of the magnet is fairly small, the pulling force and its effect are negligible. The effect of this pulling force on the operation of the system was studied via FEA. The results showed that the torsional rotation of the magnet was not affected by the force acting on the magnets. However, a negligible off-axis displacement (towards the incoming magnetic field), in the order of a few tens of nanometers, was observed.

For an ideal (neither stores nor dissipate energy) two-port gyrator [27], the electrodynamic transduction coefficient K_{T} (units of N m A^{-1} or V s rad^{-1}) is defined as

$$K_{\text{T}} = \frac{\tau_{\text{mag}}}{I_{\text{S}}} = \frac{V_{\text{mag}}}{\dot{\theta}} \quad (4)$$

where V_{mag} is the induced voltage in the transmitter coil due to the rotational motion $\dot{\theta}$ of the receiver magnet. Figure 7 plots the simulated on-axis magnetic field B_z and corresponding values of torque τ_{mag} and electrodynamic transduction coefficient K_{T} as a function of distance between the transmitter coil and the receiver. As seen from the figure, both τ_{mag} and K_{T} decrease as the magnetic field B_z decreases with the increase in the distance. In this case, a 2 mT$_{\text{rms}}$ field is generated (requiring a source current I_{S} of 872.5 mA$_{\text{rms}}$) at the centroid of the

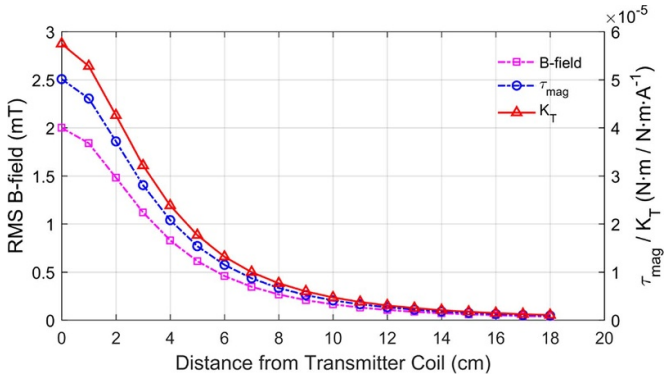

Figure 7. Simulated magnetic field and corresponding torque and the electrodynamic transduction coefficient as a function of distance from the transmitter coil while a 2 mT_{rms} magnetic field is induced at the centroid of the coil.

transmitter coil ($z = 0$), which is well below the maximum allowable human exposure limit of 2.84 mT_{rms} at 725 Hz (head and torso in controlled environment) [16].

The lumped mechanical parameters for the model are determined from the COMSOL simulations. First, J is extracted by considering the mass distribution of the oscillating body while rotating about the axis of rotation A–A′ (see figure 2(a)). Next, the short-circuit and open-circuit torsional stiffnesses are estimated from the system resonant frequencies, i.e. $k = J(2\pi f_{r-sc})^2$ and $k_0 = J(2\pi f_{r-oc})^2$, respectively. κ^2 represents the electromechanical coupling factor, which is determined from the short-circuit f_{r-sc} and open-circuit f_{r-oc} resonant frequencies

$$\kappa^2 = 1 - (f_{r-sc}/f_{r-oc})^2. \tag{5}$$

Note also, $k = \left(1-\kappa^2\right) k_0$ [28].

Since the receiver has two identical unimorph piezoelectric transducers of free electrical capacitance C_p connected in series, $C = C_p/2$ represents their equivalent series capacitance. Now, the value of blocked/clamped electrical capacitance C_0 can be determined by [29]

$$C_0 = \left(1-\kappa^2\right) C = \left(1-\kappa^2\right) \frac{\in_0 wl}{2t_p} \in_{33}^S \tag{6}$$

where w, l, and t_p are the width, length and thickness of the piezo-ceramic element, respectively; $\in_0$ (=8.854 × 10^{-12} F m^{-1}) is the permittivity of free space; $\in_{33}^S$ is the permittivity component at constant strain with the plane-stress assumption of a thin beam. Finally, the transformer turn ratio Γ_P (in N m V^{-1}) can be determined by

$$\Gamma_P = \sqrt{\kappa^2 kC}. \tag{7}$$

2.4. Performance analysis

In order to analyze the output performance and compare with experimental results later, a simplified equivalent circuit model of the piezoelectric receiver, as shown in figure 8, is used. First, an ideal torque source is considered since the

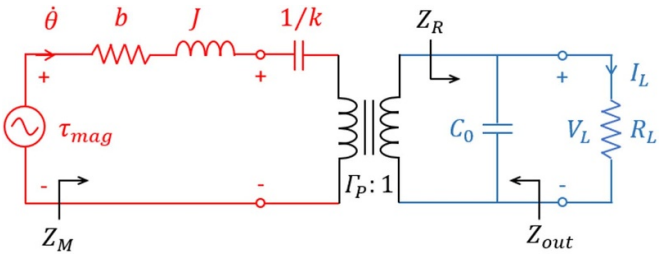

Figure 8. Simplified equivalent electrical circuit of the piezoelectric receiver with a resistive load.

torque τ_{mag} generated by the transmitted magnetic field source (transmitter coil) is well controlled during the experiments. Second, the complex load impedance Z_L is replaced with a resistive load R_L for the sake of simplicity. As indicated in the circuit diagram, Z_M and Z_{out} represent the mechanical and total output impedances of the electromechanically coupled system, respectively, whereas Z_R is the total electrical impedance of the piezoelectric transducer plus load.

Applying standard ac circuit analysis, the frequency-dependent voltage across an arbitrary load resistance R_L can be obtained (see appendix for derivation) as

$$V_L = \frac{\Gamma_P \tau_{mag}}{\left(b + j\omega J + \frac{k}{j\omega}\right)(1 + j\omega C_0 R_L) + \Gamma_P^2 R_L} R_L. \tag{8}$$

Three special cases are considered and discussed below to explicitly describe the performance of the piezoelectric receiver under various harmonic excitation and load conditions.

2.4.1. Case I: no-load condition. In the absence of any external load connected to the transducer, the frequency-dependent no-load (open-circuit) voltage output of the receiver is

$$V_L|_{R_L \to \infty} = \frac{\Gamma_P \tau_{mag}}{j\omega C_0 \left(b + j\omega J + \frac{k}{j\omega}\right) + \Gamma_P^2}. \tag{9}$$

2.4.2. Case II: at resonance. When $\omega = \omega_{r-oc}$, the rotational displacement and angular velocity (for a given load resistance) of the magnet-mass is maximized, since the impedances due to torsional spring stiffness k and mass moment of inertia J cancel. As a result, maximum stress is generated in the piezo-ceramic elements and, therefore, the load voltage and time-average power delivered to the connected load is maximized. In this case,

$$V_L|_{\omega=\omega_{r-oc}} = \frac{\Gamma_P \tau_{mag}}{b\left(1 + j\omega_{r-oc} C_0 R_L\right) + \Gamma_P^2 R_L} R_L \tag{10}$$

$$P_L|_{\omega=\omega_{r-oc}} = \frac{V_L^2}{R_L} \tag{11}$$

where V_L and τ_{mag} are both root-mean-square (rms) values.

Table 1. System parameters used for analytical simulation.

Parameter	Value
Inner diameter of the transmitter coil, d_1	5 cm
Outer diameter of the transmitter coil, d_2	15 cm
Thickness of the transmitter coil, l	1.5 cm
Resistance of the transmitter coil, R_T	305 mΩ
Inductance of the transmitter coil, L_T	2.6 mH
No. of turns in the transmitter coil, N	169
Volume of the receiver magnet, v_{mag}	2.5×10^{-8} m^3
[a]Residual flux density of the magnet, B_r	1.26 T
Length of piezo-ceramic layer, l	5 mm
Width of piezo-ceramic layer, w	1 mm
Thickness of piezo-ceramic layer, t_p	127 μm
Thickness of suspension base, t_s	125 μm
Permittivity component at constant strain, $\in_{33}^{S}$	1800
Capacitance of piezo elements in series, C	314 pF
Torsional mass moment of inertia, J	4.96×10^{-10} Kg m^2
Torsional spring stiffness (open-circuit), k_0	1.03×10^{-2} N m rad^{-1}
Electromechanical coupling coefficient, κ^2	4.07×10^{-3}
Transformer turn ratio, Γ_P	1.18×10^{-7} N m V^{-1}
Mechanical quality factor, Q	60
Mechanical damping ratio, ζ	0.008
Torsional damping coefficient, b	3.76×10^{-8} N m s rad^{-1}

[a] The value 1.26 T used here is 10% less than the datasheet value (1.40 T) since the magnet has a nickel coating that comprises ∼10% of the physical magnet volume.

2.4.3. Case III: at resonance with optimal resistive load. The load power can be maximized by choosing an impedance-matched optimal load resistance. The value of optimal load resistance is equal to the magnitude of the total output electrical impedance at the receiver terminals which, at resonance $(\omega = \omega_{r-oc})$, is

$$R_{L\_opt} = |Z_{out}| = \frac{b}{\sqrt{\left(\Gamma_P^2\right)^2 + \left(\omega_{r-oc} C_0 b\right)^2}}. \quad (12)$$

Therefore, the corresponding load voltage and maximum time-average power to the load resistance become

$$V_{opt} = V_L|_{\substack{\omega = \omega_{r-oc} \\ R_L = R_{L\_opt}}} = \frac{\Gamma_P \tau_{mag}}{2\sqrt{\left(\Gamma_P^2\right)^2 + \left(\omega_{r-oc} C_0 b\right)^2}} \quad (13)$$

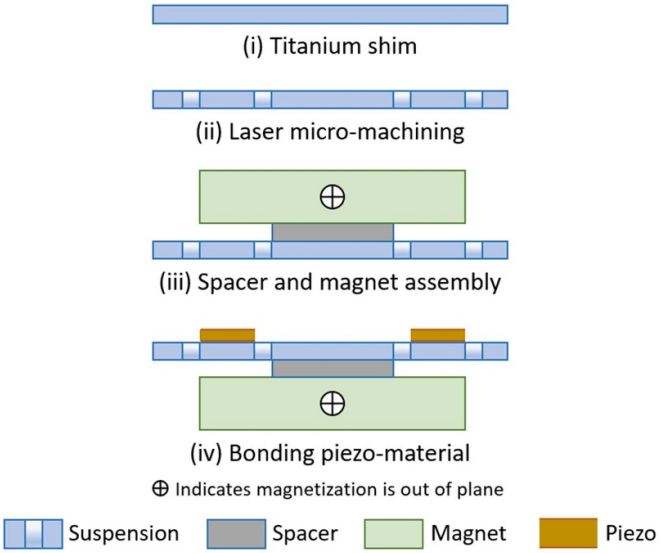

Figure 9. Schematics of the piezoelectric receiver fabrication and assembly process steps.

$$P_{max} = P_L|_{\substack{\omega = \omega_{r-oc} \\ R_L = R_{L\_opt}}} = \frac{\Gamma_P^2 \tau_{mag}^2}{4b\sqrt{\left(\Gamma_P^2\right)^2 + \left(\omega_{r-oc} C_0 b\right)^2}}. \quad (14)$$

Table 1 shows the parameters used in the analytical calculation, derived from the geometry and material properties of the components used in the proposed EWPT system.

3. Prototype fabrication

A receiver prototype was fabricated and assembled to test under various magnetic fields with resistive loads. Figure 9 shows the schematics of the fabrication and assembly process steps. The meandering suspension structure with surrounding anchor base was formed by laser micro-machining 125 μm-thick titanium (Ti) shim stock (McMaster-Carr, IL, USA). The width of the meandered beam is 1 mm, and the area of the center platform is 2.6 × 2.6 mm^2. A same sized silicon (Si) spacer, diced out of a 200 μm-thick, double-side polished Si wafer (University Wafer, Inc., MA, USA) and a laterally magnetized 5 ×5 × 1 mm^3 N50 NdFeB (Super Magnet Man, AL, USA) magnet were bonded using cyanoacrylate to one side of the center platform. On the opposite side, two piezo-ceramic patches, each 5 ×1 × 0.127 mm^3, diced from a large PZT-5A sheet with sputtered Nickel electrodes and poled through thickness (Piezo.com, MA, USA), were bonded to the arms of the meandered beam using silver epoxy (EO-21M-5, EpoxySet Inc., RI, USA) to form a series electrical connection between two unimorph piezo-ceramic transducers. Finally, the surrounding anchor base of the assembled device was clamped to a 3D printed plastic base, and the output electrical connections were created by bonding thin copper wires using silver epoxy, as shown in figure 10.

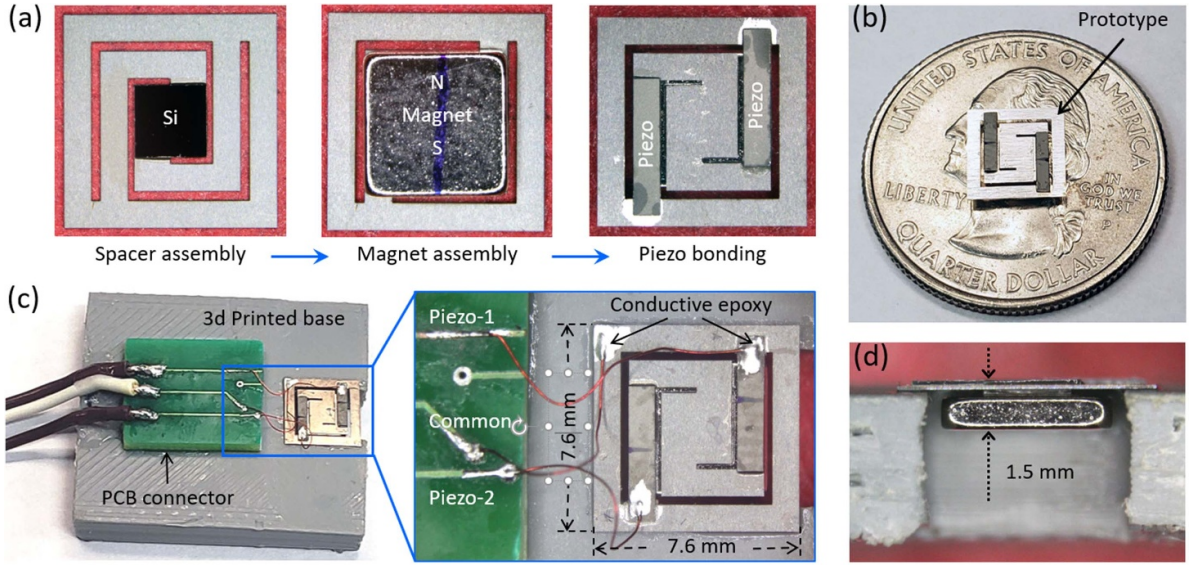

Figure 10. Photographs of (a) the receiver assembly process steps, (b) a fully assembled prototype with size compared to a US quarter dollar, (c) the prototype mounted to a 3D-printed plastic base and (d) the corresponding cross-section view showing the 1.5 mm device thickness.

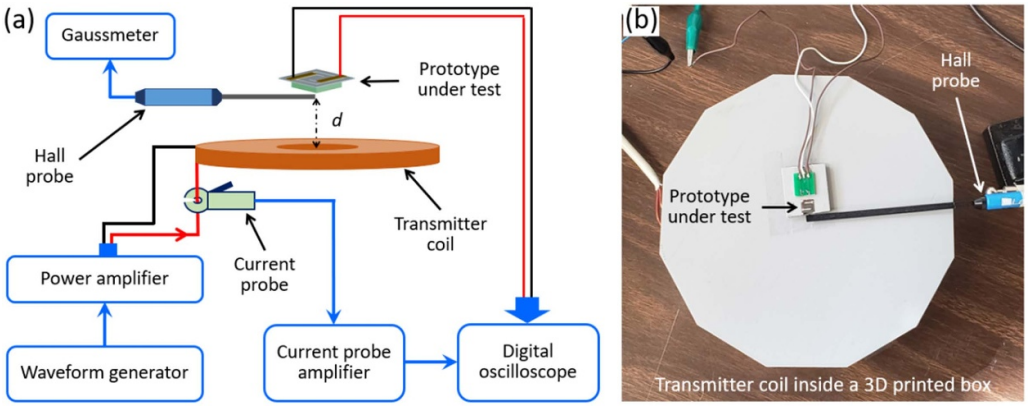

Figure 11. (a) Schematic block diagram and (b) a photograph of the experimental characterization of the fully assembled EWPT piezoelectric receiver prototype.

4. Experimental characterization

4.1. Experimental setup

The fully assembled piezoelectric receiver prototype was tested under various alternating magnetic fields transmitted from the transmitter coil. Figure 11 shows the block diagram and a photograph of the experimental setup. The receiver prototype was placed on the top surface (at the center) of a 3D printed plastic cover that covers the transmitter coil. The distance between the receiver and transmitter (d) was varied by changing the height between the plastic cover and the coil. The transmitter coil (Ø150 mm $\times$ 15 mm) is made of 169 turns of 12 AWG copper magnet wire. It generates uniaxial, time-varying fields and has 13.4 $\times$ 10^6 W T^{-2} coil figure-of-merit [21]. A waveform generator (Rigol DG1022A) in conjunction with a power amplifier (Crown K1) supplied an alternating current input into the transmitter coil, which was monitored by a current probe (Tektronix TCP312A) connected to a current probe amplifier (Tektronix TCPA300). An oscilloscope (Tektronix DPO-2004B) was used to measure the input current to the transmitter coil and the output voltage generated by the receiver prototype. For a given alternating current of the transmitter coil, the resultant B-field spatial distribution was measured by a gaussmeter (Lakeshore 475DSP) via a transverse Hall probe (Lakeshore HMNT-4E04-VR).

4.2. Results and discussion

The 1st mode torsional resonance of the receiver was first determined from the frequency response curves by measuring the no-load rms voltages as a function of the frequency of the applied magnetic field. In this first set of experiments, an axial distance $d = 2$ cm was maintained between the face of the receiver magnet and the centroid of the transmitter coil.

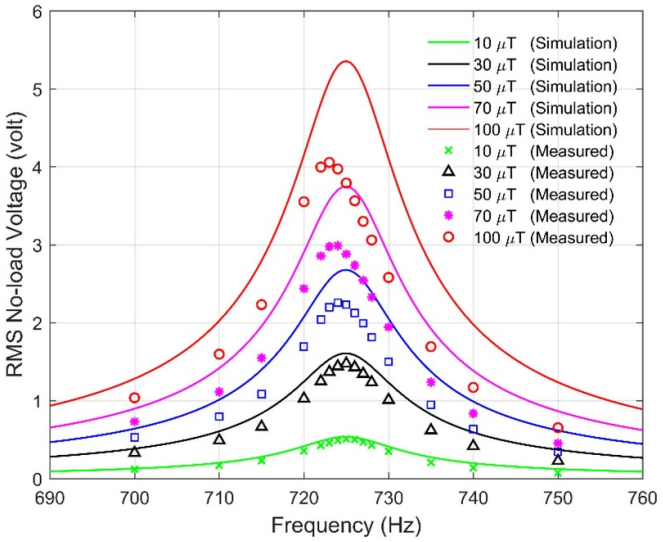

Figure 12. No-load voltage vs. frequency for various magnetic fields transmitted from the transmitter coil, at 2 cm axial distance.

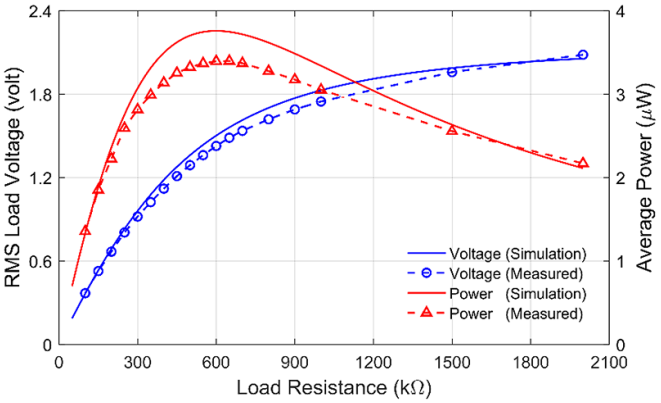

Figure 13. Load voltage and power vs. load resistance under 50 μT_{rms} magnetic field (at 2 cm axial distance) at resonance.

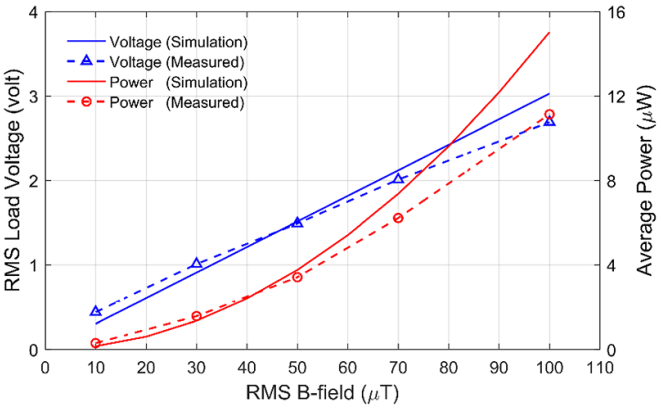

Figure 14. Power (and voltage) delivered to 650 kΩ optimum load under various magnetic fields (at 2 cm axial distance) at resonance.

Figure 12 shows both simulation (solid lines) and measurement (markers) results under various magnetic fields. The field amplitudes (between 10 and 100 μT_{rms}) of desired frequencies at the receiver magnet location were achieved by adjusting the ac current (between 6 and 59 mA_{rms}) supplied to the transmitter coil. The prototype device exhibits a characteristic peak at its resonance (∼724 Hz) indicating an underdamped second-order system with Q-factor of 60 (in air). As seen from the figure, the system exhibits a slightly non-linear behavior, where the measured resonant frequency tends to shift lower as the amplitude of the magnetic field increases. The frequency of the torsional resonant frequency closely matches with the 1st mode frequency predicted by the 3D-FEA model (725 Hz).

Figure 13 shows the simulated (solid lines) and measured (dashed lines with markers) rms voltage and corresponding time-average power delivered to various load resistances (between 50 kΩ to 2 MΩ) while a 50 μT_{rms} (the current was adjusted to 31 mA_{rms}) constant-amplitude alternating magnetic field at 724 Hz resonance was maintained. The time-average power was determined by using V_{rms}^2/R_L, where V_{rms} is the rms value of the measured voltage across each load resistance R_L. Results indicate that, as expected, the rms voltage increases as the value of the load resistance increases, however, a maximum power (3.4 μW) is delivered to an optimum load resistance of 650 kΩ.

Next, the voltage across and the time-average power delivered to the previously determined optimal load resistance was measured by varying the amplitude of the alternating magnetic field, while its frequency was kept constant at 724 Hz. Figure 14 shows the simulated (solid lines) and measured (dashed lines with markers) rms voltage and time-average power as a function of magnetic fields. Simulation shows that the load voltage increases linearly, whereas the time-average power increases quadratically as the magnetic field amplitude increases. Measurement results also follow the same trend, however, both voltage and power tend to deviate from this linear trend at higher magnetic fields (over 45 μT_{rms}). The measured power reaches to 11 μW at 100 μT_{rms} magnetic field, whereas the simulation predicts 15 μW. This discrepancy occurs due to the nonlinear behavior of the receiver noticed earlier in the frequency response analysis (figure 12).

Finally, the time-average power delivered to the 650 kΩ optimum load was measured at various distances (d ranging from 1 cm to 18 cm) between the transmitter coil and the receiver prototype, as shown in figure 15. In this case, a 2 mT_{rms} magnetic field at 724 Hz frequency (below the human exposure safety limit at this frequency) was generated at the centroid of the transmitter coil by limiting the supply current at 879 mA_{rms}. Obviously, the amplitude of the magnetic field at various receiver locations decay as the distance increases. It is seen from the figure that the receiver generated maximum 360 μW power at 1 cm distance from the transmitter coil, that corresponds to 4.2 mW cm^{-3} power density. The power generation certainly decreases since the magnetic field weakens as the distance from the source increases. However, the receiver prototype was still able to generate meaningful power (24 μW) at 10 cm distance, where the magnetic field strength was measured to be 161 μT_{rms}. It is also observed from the figure that the measured power values are quite lower than those obtained via simulation particularly as the receiver is moved closer the

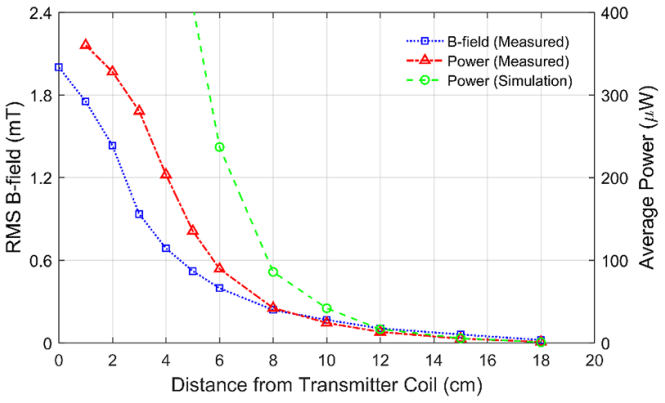

Figure 15. Measured power and magnetic field vs. axial distance between the transmitter coil and receiver prototype while a maximum allowable safe field of 2 mT_{rms} at 724 Hz was generated at the centroid of the transmitter coil.

transmitter coil i.e. the receiver is exposed to stronger fields. While the receiver operates at stronger field amplitudes, any system nonlinearities becomes more evident. Potential sources of non-linearity include mechanical spring stiffening effect and/or nonlinear piezoelectric properties. As a result, the resonant frequency moves further away from the resonance of 724 Hz at which all the measurements were taken. These nonlinear analyses are beyond the scope of this paper and will be further analyzed in a future work.

The maximum power transfer efficiency of the proposed EWPT system is ∼0.036% which is quite low as compared to that of other techniques [10]. However, the amount of power required (∼1 W) to generate low-frequency (<1 kHz) electromagnetic near-fields within the human exposure safety limit (∼2 mT_{rms}) to operate the EWPT receiver is still very low and economic. On the other hand, the amount of power generated by the EWPT receiver is sufficient enough to wirelessly charge/power an implantable medical device (e.g. cardiac pacemaker, deep brain neurostimulator, cochlear implants etc).

5. Conclusions

In this work, we have designed, modeled, fabricated and tested a laser micro-machined, low-profile EWPT receiver using two simultaneously operating, series-connected piezoelectric transducers on a torsionally resonated meandering suspension for near-field WPT, well suited for wearable and bio-implantable applications. The device can be mounted into various structures such as printed-circuit boards to seamlessly integrate the wireless power receiver with other device electronics. COMSOL finite element analyses are performed to study the modal analysis, mechanical reliability and design of the piezoelectric elements of the receiver. An equivalent lumped-element electromechanical model has also been established and well predicts the device performance. Experimental results reveal that the receiver generates maximum 360 μW time-average power at 724 Hz resonance at an axial near-field distance of 1 cm from a transmitter coil operating within IEEE safety standards for human exposure limit. Moreover, it is capable of delivering useful power at further distances such as inside the body, or deep in an enclosed product (e.g. 24 μW at 10 cm). Experimental results show good agreement with the model predictions, however, deviations are observed at higher field amplitudes (starting from 45 μT_{rms}) due to nonlinearities. As compared to a much larger previously reported prototype [24], this volume-efficient, chip-sized receiver prototype is 31× smaller (0.08 cm^3 vs. 2.5 cm^3); offers 1.7× higher Q-factor (60 vs. 35), 3.2× larger power density (4.2 mW cm^{-3} vs. 1.3 mW cm^{-3}), and 1.4× higher normalized power density (10.6 mW cm^{-3} mT^{-2} vs. 8.2 mW cm^{-3} mT^{-2}) when operating at the same distance (10 cm) from the transmitter coil.

Appendix

From the simplified equivalent electrical circuit model presented in figure 8, the angular velocity of the receiver magnet due to the driving torque τ_{mag} is given by

$$\dot{\theta} = \frac{\tau_{mag}}{Z_M} = \frac{\tau_{mag}}{\left(b + j\omega J + \frac{k}{j\omega}\right) + \Gamma_P^2 Z_R}. \tag{A1}$$

where Z_R in the mechanical impedance Z_M of the receiver reads as

$$Z_R = \frac{\frac{1}{j\omega C_0} R_L}{\frac{1}{j\omega C_0} + R_L} = \frac{R_L}{1 + j\omega C_0 R_L}. \tag{A2}$$

Now, according to a lossless two-port transducer principle (in this case, the transformer and two capacitances $1/k$ and C_0) [28], the voltage across the load resistance R_L

$$V_L = \frac{\tau_{mag} - \left(b + j\omega J + \frac{k}{j\omega}\right)\dot{\theta}}{\Gamma_P}. \tag{A3}$$

Substituting (A2) and (A1) into (A3) yields

$$V_L = \frac{\Gamma_p \tau_{mag}}{\left(b + j\omega J + \frac{k}{j\omega}\right)(1 + j\omega C_0 R_L) + \Gamma_P^2 R_L} R_L. \tag{A4}$$

The total electrical output impedance Z_{out} at the receiver output terminals is

$$Z_{out} = \frac{\frac{1}{j\omega C_0}\left[\frac{1}{\Gamma_P^2}\left(b + j\omega J + \frac{k}{j\omega}\right)\right]}{\frac{1}{j\omega C_0} + \left[\frac{1}{\Gamma_P^2}\left(b + j\omega J + \frac{k}{j\omega}\right)\right]}. \tag{A5}$$

Acknowledgments

This work was supported in part by the NSF I/UCRC on Multi-functional Integrated System Technology (MIST) Center (NSF Grant IIP-1439644, IIP-1439680, and IIP-1738752).

ORCID iDs

Miah A Halim https://orcid.org/0000-0003-3879-9017
David P Arnold https://orcid.org/0000-0003-2515-7218

References

[1] Garnica J, Chinga R A and Lin J 2013 Wireless power transmission: from far field to near field *Proc. IEEE* **101** 1321–31

[2] Song M, Belov P and Kapitanova P 2017 Wireless power transfer inspired by the modern trends in electromagnetics *Appl. Phys. Rev.* **4** 021102

[3] Huang J, Zhou Y, Ning Z and Gharavi H 2019 Wireless power transfer and energy harvesting: current status and future prospects *IEEE Wireless Commun.* **26** 163–9

[4] Al-Attar A, Attia S A, Al-Bialy A, Abdelatif E N, Al-Gazar A S, Salem A and Badr B M 2019 Wireless power transfer for toys and portable devices pp 479–84

[5] Subudhi P S and Krithiga S 2020 Wireless power transfer topologies used for static and dynamic charging of EV battery: a review *Int. J. Emerging Electr. Power Syst.* **21** 20190151

[6] Khan S R, Pavuluri S K, Cummins G and Desmulliez M P Y 2020 Wireless power transfer techniques for implantable medical devices: a review *Sensors* **20** 3487

[7] Dekimpe R, Xu P, Schramme M, Gérard P, Flandre D and Bol D 2019 A battery-less BLE smart sensor for room occupancy tracking supplied by 2.45-GHz wireless power transfer *Integration* **67** 8–18

[8] Yang C, He Y, Qu H, Wu J, Hou Z, Lin Z and Cai C 2019 Analysis, design and implement of asymmetric coupled wireless power transfer systems for unmanned aerial vehicles *AIP Adv.* **9** 025206

[9] Putra A W S, Tanizawa M and Maruyama T 2019 Optical wireless power transmission using Si photovoltaic through air, water, and skin *IEEE Photonics Technol. Lett.* **31** 157–60

[10] Taalla R V, Arefin M S, Kaynak A and Kouzani A Z 2019 A review on miniaturized ultrasonic wireless power transfer to implantable medical devices *IEEE Access* **7** 2092–106

[11] Garraud A and Arnold D P 2016 Advancements in electrodynamic wireless power transmission *IEEE Sensors Conf.* pp 82–4

[12] Zhang Z, Pang H, Georgiadis A and Cecati C 2019 Wireless power transfer- an overview *IEEE Trans. Ind. Electron.* **66** 1044–58

[13] Jawad A M, Nordin R, Gharghan S K, Jawad H M and Ismail M 2017 Opportunities and challenges for near-field wireless power transfer: a review *Energies* **10** 1022

[14] Ding-Xin Y, Zheng H, Hong Z, Hai-Feng H, Yun-Zhe S and Bao-Jian H 2015 Through-metal-wall power delivery and data transmission for enclosed sensors: a review *Sensors* **15** 31581–605

[15] IEEE 2010 Standard for safety levels with respect to human exposure to radio frequency electromagnetic fields, 3 kHz to 300 GHz *IEEE Std. C95.1a-2010* pp 1–238

[16] IEEE 2002 Standard for safety levels with respect to human exposure to electromagnetic fields, 0–3 kHz *IEEE Std. C95.6–2002* pp 1–43

[17] Li W 2009 High efficiency wireless power transmission at low frequency using permanent magnet coupling MS Thesis Department of Physics and Astronomy, University of British Columbia, Vancouver, Canada

[18] Challa V R, Mur-Miranda J O and Arnold D P 2012 Wireless power transmission to an electromechanical receiver using low-frequency magnetic fields *Smart Mater. Struct.* **21** 115017

[19] Du S, Chan E K, Wen B, Hong J, Widmer H and Wheatley C E 2018 Wireless power transfer using oscillating magnets *IEEE Trans. Ind. Electron.* **65** 6259–69

[20] Paprotny I, Waterbur A, Challa V R, Xu Q, Arnold D P, Sanders S and Wright P K 2012 Piezoelectrodynamic gyrator: analysis, experiments, and applications to wireless power transfer *19th Int. Conf. on Micro and Nanotechnology for Power Generation and Energy Conversion Applications (PowerMEMS)* pp 263–6

[21] Garraud N, Alabi D, Chyczewski S, Varela J D, Arnold D P and Garraud A 2018 Extending the range of wireless power transmission for bioimplants and wearables *J. Phys.: Conf. Ser.* **1052** 012023

[22] Garraud N, Munzer D, Althar M and Arnold D P 2019 Modeling and experimental analysis of rotating magnet receivers for electrodynamic wireless power transmission *J. Phys. D: Appl. Phys.* **52** 185501

[23] Halim M A, Smith S E, Samman J M and Arnold D P 2020 A high-performance electrodynamic receiver for low-frequency wireless power transfer *33rd IEEE Int. Conf. on Micro Electro Mechanical Systems (IEEE MEMS)* pp 590–3

[24] Halim M A, Samman J M, Smith S E and Arnold D P 2019 Piezoceramic electrodynamic wireless power receiver using torsion mode meandering suspension *19th Int. Conf. on Micro and Nanotechnology for Power Generation and Energy Conversion Applications (PowerMEMS)* pp 1–5

[25] Truong B D, Williams S and Roundy S 2019 Experimentally validated model and analytical investigations on power optimization for piezoelectric-based wireless power transfer systems *J. Intell. Mater. Syst. Struct.* **30** 2464–77

[26] Truong B D and Roundy S 2019 Wireless power transfer system with center clamped magneto-mechano-electric (MME) receiver: model validation and efficiency investigation *Smart Mater. Struct.* **28** 015004

[27] Senturia S D 2001 *Microsystem Design* (New York: Kluwer Academic Publishers)

[28] Tilmans H A C 1996 Equivalent circuit representation of electromechanical transducers: I. Lumped-parameter systems *J. Micromech. Microeng.* **6** 157–76

[29] Williams M D, Griffin B A, Reagan T N, Underbrink J R and Sheplak M 2012 An AlN MEMS piezoelectric microphone for aeroacoustic applications *J. Microelectromech. Syst.* **21** 270–83